Doppler-broadened quantum electromagnetically-induced-transparency heat engines

Xiao-Jun Zhang ●,[1] G. C. La Rocca,[2,*] M. Artoni,[3,4,†] Hai-Hua Wang,[5] and Jin-Hui Wu[1,‡]

[1]*School of Physics, Northeast Normal University, Changchun 130024, China*
[2]*Scuola Normale Superiore and CNISM, 56126 Pisa, Italy*
[3]*European Laboratory for Nonlinear Spectroscopy, 50019 Firenze, Italy*
[4]*National Institute Optics (National Research Council), 50019 Firenze, Italy*
[5]*College of Physics, Jilin University, 130023 Changchun, China*

A nontraditional quantum heat engine based on electromagnetically induced transparency has recently been suggested and experimentally demonstrated in ultracold atoms. In more practical setups with warm atoms, thermal atomic motions might hamper this heat engine mechanism. We here show that a Doppler-broadened atomic sample can still behave like an engine. However, only photons emitted in the direction of the coupling laser have the same brightness as for the Doppler-free engine, while the larger the angular deviation of emission, the lower the brightness. Our results suggest that the lower brightness can be seen as an act of Doppler broadening as if the thermal occupation number of the reservoir serving as entropy sink is increased, and the quantum heat engines may be feasible in warm atomic interfaces.

I. INTRODUCTION

Atomic coherence built in the interaction between lasers and atomic ensembles is the basis of a well-known phenomenon called electromagnetically induced transparency (EIT). Many related effects have been intensively studied, such as lasing without inversion [1], slow and stored light [2,3], stationary light pulses [4], entangled photon pairs [5], and quantum gates [6,7]. In 2016 [8], in particular, Harris showed that, under the coupling laser beam (Ω_c), a lambda EIT medium in contact with two blackbody reservoirs at temperatures T_{13} and T_{23} supports a nonlinear process $|1\rangle \xrightarrow{T_{13}} |3\rangle \xrightarrow{T_{23}} |2\rangle \xrightarrow{\Omega_c} |3\rangle \xrightarrow{\Omega_p} |1\rangle$ which can be regarded as a heat engine cycle [see Fig. 1(a)]. The atoms, in fact, convert heat from the first reservoir (T_{13}), releasing some of it into the other reservoir (T_{23}) while generating low-grade work at the (output) photon mode at Ω_p. The entropy change associated with photon absorption from the *ideal* laser beam (Ω_c) is zero [9] and the brightness of the generated radiation, i.e., the number of photons generated in the mode Ω_p, is larger than what one would obtain in the presence of the two reservoirs alone [8]. Such a nontraditional EIT-based engine has been experimentally demonstrated in ultracold samples of ^{85}Rb atoms [10], where Doppler broadening is absent.

Doppler broadening, which is caused by the random thermal motion of atoms, is nevertheless present in warm atom platforms that are routinely used to achieve light dragging [11], optical nonreciprocity [12–15], and narrowband biphoton generation [16], just to name a few phenomena. Actual implementations of an atomic heat engine would also benefit from using warm atoms due to the simplicity and convenience in their preparation and manipulation, yet in most cases Doppler broadening is known to play a hampering role because averaging over the atom velocities could wash out fragile quantum coherent effects. Hence the effect of the atomic thermal motion on the engine performance has to be properly assessed.

We discuss here a quantum heat engine designed to work with a warm atomic gas (see Fig. 1) through the inclusion of Doppler broadening in the model of Ref. [8]. We limit ourselves to a two-dimensional (2D) space, which is the simplest extension to a configuration that provides a detailed quantitative analysis with respect to the effects of the atomic motion on the behavior of an EIT-based engine. Doppler-broadened transitions are well known to exhibit a *Gaussian lineshape* profile (Maxwell-Boltzmann distribution) and this is first used to numerically compute the brightness of the output radiation. A deeper insight into the role of Doppler broadening is instead gained by adopting a *Lorentzian lineshape* profile [17–19] which leads to useful, although approximate, analytic expressions for the brightness. Both numerical and analytic results for a thermal sample anticipate a reduction of the brightness distribution over the emission angle as one moves away from the forward direction [see Fig. 1(b)], findings that are quite relevant to practical experimental implementations. The Lorentzian case, in addition, yields a sound physical understanding of how the broadening causes such a reduction. Finally, we discuss the heat engine performance in terms of the entropy flux carried by the output radiation [8,9,20,21].

II. BRIGHTNESS OF THE DOPPLER-BROADENED QUANTUM HEAT ENGINE

Let us consider the atomic system depicted in Fig. 1(a) where three-level atoms are in contact with two (*blackbody*)

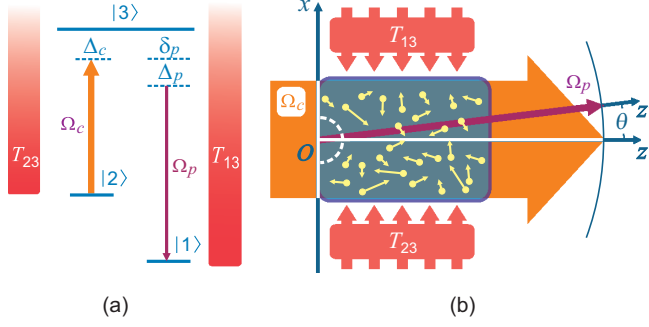*giuseppe.larocca@sns.it
†artoni@lens.unifi.it
‡jhwu@nenu.edu.cn

FIG. 1. Doppler-broadened quantum EIT heat engine: (a) Three-level atoms generate the field Ω_p (purple arrow) as output in the presence of thermal radiation from two black-bodies of different temperatures (red shapes) and of a coherent coupling field Ω_c (orange arrow). (b) Owning to the thermal motion of the atoms, the brightness of the output is not isotropic—it depends on the angle θ between the traveling direction of the output field and the z axis along which the laser beam Ω_c propagates. The atoms are contained in a two-dimensional cell the size of which is much larger than the characteristic length ξ_o, represented by the white semicircular dashed line, over which the output field reaches its asymptotic value (see Sec. II).

reservoirs at temperatures T_{13} and T_{23}. The reservoirs thermal occupation numbers are, as usual, $\bar{n}_{13} = [\exp(\hbar\omega_{13}/K_b T_{13}) - 1]^{-1}$, $\bar{n}_{23} = [\exp(\hbar\omega_{23}/K_b T_{23}) - 1]^{-1}$ so that, if we denote by Γ_{31} and Γ_{32} the upper level decay rates, one has for the pumping rates,

$$R_{13} = \Gamma_{31}\bar{n}_{13}, \tag{1a}$$

$$R_{23} = \Gamma_{32}\bar{n}_{23}. \tag{1b}$$

The transition $|3\rangle \leftrightarrow |2\rangle$ is further driven by a classical *coupling* field at frequency ω_c and wave vector $\mathbf{k_c}$ that defines the **z** axis, as shown in Fig. 1(b). The heat engine, operated by the coupling field and the two reservoirs [8], generates output radiation (work) at frequency ω_p which is collected at an angle θ with respect to **z**.

We take a cell of warm atoms moving, for the sake of simplicity, in the xz plane, where $\hat{\mathbf{e}}_z$ ($\hat{\mathbf{e}}_x$) is a unit vector along (perpendicular to) the direction of the coupling field. Then, for an atom moving at speed $\mathbf{v} = v_x\hat{\mathbf{e}}_x + v_z\hat{\mathbf{e}}_z$, the Doppler effect amounts to a frequency shift (Δ_c and Δ_p) for the coupling and output fields (Ω_c and Ω_p), respectively,

$$\Delta_c(v_z) = -k_c v_z, \tag{2a}$$

$$\Delta_p(v_x, v_z) = -k_{px}v_x - k_{pz}v_z. \tag{2b}$$

Here $k_c = \omega_c/c$, $k_{px} = k_p\sin\theta$, $k_{pz} = k_p\cos\theta$, and $k_p = \omega_p/c$. The Doppler shifts contribute through the *complex* decoherence rates $\tilde{\gamma}_{21} = \frac{\gamma_{21}}{2} - i[\delta_p + \Delta_p(v_x, v_z) - \Delta_c(v_z)]$, $\tilde{\gamma}_{31} = \frac{\gamma_{31}}{2} - i[\delta_p + \Delta_p(v_x, v_z)]$, and $\tilde{\gamma}_{32} = \frac{\gamma_{32}}{2} - i\Delta_c(v_z)$. The difference between the frequency of the output field ω_p and the transition frequency ω_{31} is $\delta_p = \omega_p - \omega_{31}$, while the detuning of the coupling field ($\omega_c - \omega_{32}$) is here assumed to

be vanishing, i.e., for the stationary atom ($\mathbf{v} = 0$), the coupling field is resonant with the $|3\rangle \leftrightarrow |2\rangle$ transition. The *real* decay rates are defined instead as $\gamma_{21} = \gamma_0 + R_{13} + R_{23}$, $\gamma_{31} = \Gamma_{31} + \Gamma_{32} + R_{23} + 2R_{13}$, and $\gamma_{32} = \Gamma_{31} + \Gamma_{32} + R_{13} + 2R_{23}$, where γ_0 represents the decoherence effect due to collisions and/or time-of-flight broadening (we do not include this contribution in γ_{31} and γ_{32} as in any case it would be negligible compared with Γ_{31} and Γ_{32}). If we assume that the generated output field (Ω_p) is *weak*, the Liouville equations for the atomic density-matrix elements ρ_{ij} can be solved for the populations to zeroth order in Ω_p, obtaining

$$\rho_{11}^{(0)} = \frac{X(\Gamma_{31} + R_{13})}{X(\Gamma_{31} + 3R_{13}) + \Gamma_{32}R_{13}}, \tag{3a}$$

$$\rho_{22}^{(0)} = \frac{R_{13}(\Gamma_{32} + X)}{X(\Gamma_{31} + 3R_{13}) + \Gamma_{32}R_{13}}, \tag{3b}$$

$$\rho_{33}^{(0)} = \frac{R_{13}X}{X(\Gamma_{31} + 3R_{13}) + \Gamma_{32}R_{13}}, \tag{3c}$$

with $X = R_{23} + (\gamma_{32}\Omega_c^2)/(\gamma_{32}^2 + 4\Delta_c^2)$. The absorption and emission coefficients for the generated field can then be derived to first order in Ω_p from $\mathrm{Im}[\rho_{31}]$, i.e.,

$$c_{abs} = \mathrm{Im}\left[\frac{i\tilde{\gamma}_{21}\gamma_{31}}{\frac{\Omega_c^2}{2} + 2\tilde{\gamma}_{21}\tilde{\gamma}_{31}} \rho_{11}^{(0)} \right], \tag{4a}$$

$$c_{em} = \mathrm{Im}\left[\frac{(4i\tilde{\gamma}_{21}\tilde{\gamma}_{32}^* - i\Omega_c^2)\gamma_{31}\rho_{33}^{(0)} + i\Omega_c^2\gamma_{31}\rho_{22}^{(0)}}{2(\Omega_c^2 + 4\tilde{\gamma}_{21}\tilde{\gamma}_{31})\tilde{\gamma}_{32}^*} \right], \tag{4b}$$

where the Rabi frequency for the coupling (Ω_c) and output field (Ω_p) are defined as $\Omega_c = \wp_{32}E_c/\hbar$ and $\Omega_p = \wp_{31}E_p/\hbar$, where $\wp_{32}$ ($\wp_{31}$) is the dipole moment for the transition $|3\rangle \leftrightarrow |2\rangle$ ($|3\rangle \leftrightarrow |1\rangle$), and E_c, E_p stand for the corresponding electric field. The number of photons in the output mode (Ω_p), which defines here the output field *brightness B*, in the presence of Doppler broadening will also depend on the direction upon which photons are generated [see Fig. 1(b)] and satisfies the equation [8,22]

$$\frac{dB(\delta_p, \theta, \xi)}{d\xi} + [\langle c_{abs}\rangle_{xz} - \langle c_{em}\rangle_{xz}]B(\delta_p, \theta, \xi) = \langle c_{em}\rangle_{xz}. \tag{5}$$

We introduced the dimensionless position $\xi = \kappa_0 z$, where $\kappa_0 = 2k_p\omega_N/\gamma_{31}$ and $\omega_N = N_0|\wp_{31}|^2/\epsilon_0\hbar$ while $\langle c_{abs}\rangle_{xz}$ and $\langle c_{em}\rangle_{xz}$ are the absorption and emission coefficients averaged over the velocity distribution. The symbols $\langle\cdots\rangle_{xz}$ here and $\langle\cdots\rangle_x$ which appear in the following discussion stand for $\int_{-\infty}^{\infty} dv_z \int_{-\infty}^{\infty} dv_x f(v_z)f(v_x)\cdots$ and $\int_{-\infty}^{\infty} dv_x f(v_x)\cdots$, respectively. The function $f(v_i)$ with $i \in \{x, z\}$ models the velocity distribution. For a Maxwell thermal distribution with most probable speed $v_T = \sqrt{2KT/M}$,

$$f_G(v_i) = \frac{1}{v_T\sqrt{\pi}}e^{-v_i^2/v_T^2}, \tag{6}$$

and under the boundary condition $B(\delta_p, \theta, 0) = 0$ the solution of Eq. (5) can be written as

$$B(\delta_p, \theta, \xi) = \frac{\langle c_{em}\rangle_{xz}}{\langle c_{abs}\rangle_{xz} - \langle c_{em}\rangle_{xz}}\{1 - \exp[-\langle c_{abs} - c_{em}\rangle_{xz}\xi]\} \equiv B(\delta_p, \theta, \infty)\{1 - e^{-\xi/\xi_0}\}, \tag{7}$$
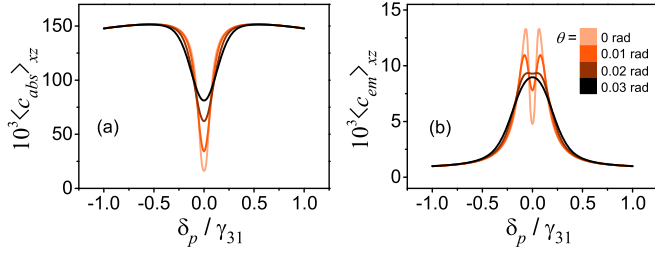
FIG. 2. The averaged (a) absorption and (b) emission coefficients: The different curves correspond to different angles θ. The Gaussian Doppler broadening f_G is employed with $kv_T = 5\gamma_{31}$, and $\Omega_c = \gamma_{31}$, $T_{13} = 4000$ K, $T_{23} = 5000$ K. The atomic parameters are appropriate for the ^{87}Rb D$_2$ line: $\Gamma_{31} = \Gamma_{32} = 2\pi \times 6$ MHz, $\gamma_0 = 2\pi \times 16$ kHz, $\lambda_{31} = 780$ nm, and $\omega_{21} = 2\pi \times 6.8$ GHz.

suggesting that there exists a *characteristic length* $\xi_0 = 1/\langle c_{abs} - c_{em}\rangle_{xz}$ for which B when $\xi \gg \xi_0$ reduces to its asymptotic value $B(\delta_p, \theta, \infty)$.

Figure 2 shows the averaged absorption and emission coefficients with $f_G(v_i)$ employed as $f(v_i)$. Treated as functions of δ_p, the coefficients are plotted under different propagation angles $\theta = 0$, 0.01, 0.02, 0.03 rad, respectively. Figure 2(a) shows that, when θ gets larger, moving away from the two-photon resonance Doppler-free configuration, the absorption at the center of the EIT window increases. This is mainly due to an additional dephasing rate dependent on the propagation angle θ and nearly proportional to $kv_T\theta$. Furthermore, Fig. 2(b) shows that, as θ increase from 0 to 0.03 rad, the two peaks of the emission coefficient merge into one while its maximum value keeps decreasing [see the lines corresponding to $\theta = 0.02$ to 0.03 rad in Fig. 2(b)], due to the same reason as for the increasing absorption.

The corresponding brightness $B(\delta_p, \theta, \infty)$ is plotted in Fig. 3 as a function of δ_p and θ: It is symmetric with respect to both δ_p (we are using $\omega_c = \omega_{23}$) and θ, in particular, decreases quickly with increasing emission angle when the Doppler broadening gets larger. Considering a field that originates from the origin and propagates along the z' axis [see Fig. 1(b)], experiencing both stimulated emission and stimulated absorption, one can easily see that the brightness of the generated field at a certain distance from the origin acquires a peaked distribution over the angle θ. This is shown in Fig. 4(a) where the relative brightness of the *resonant*
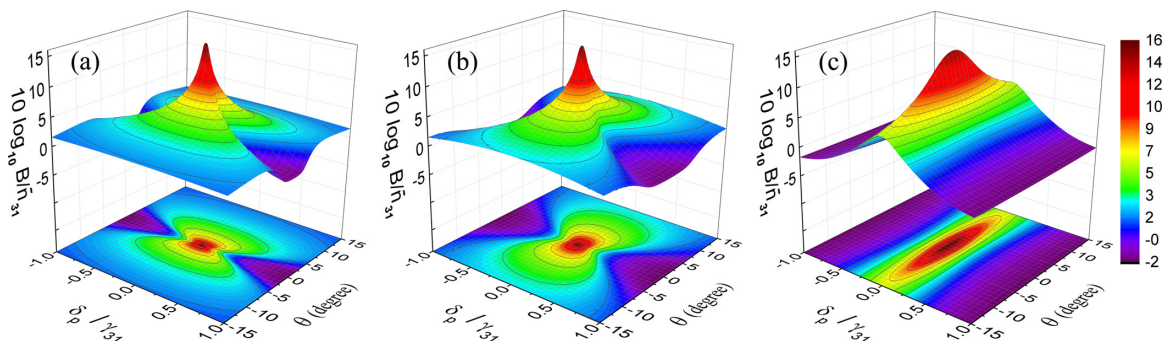

FIG. 4. (a) The ξ-θ dependence of the relative brightness $B_0/\bar{n}_{13}$. The Doppler broadening is set to $kv_T = 5\gamma_{31}$ and $\Omega_c = 1.3\gamma_{31}$, which is equivalent to $w = v_T$ [being the parameter w given in Eq. (9)], and the Gaussian-broadening function $f_G(v_i)$ is adopted in the calculation. (b) Relation between w and Ω_c (green solid line) with $kw = 5\gamma_{31}$ marked by the pink horizontal line. (c) Brightness obtained from analytic result (10) presented as a function of θ (red solid line). The numerical results with $f_G(v_i)$ (gray solid line) and $f_L(v_i)$ (black dotted line) modeling the Doppler broadening are plotted for comparison. $kv_T = 5\gamma_{31}$, and $w = v_T$ just as in panel (a). The other parameters are identical with that in Fig. 2.

output field $B(0, \theta, \xi)/\bar{n}_{13}$ is presented as a function of θ and the dimensionless position ξ (from zero to the characteristic length ξ_0).

III. LORENTZIAN LINESHAPE APPROXIMATION

It would now be instructive to obtain an approximate analytical expression for the brightness by modeling the inhomogeneous broadening through a Lorentzian lineshape profile, i.e.,

$$f_L(v_i) = \frac{v_T}{\pi\left(v_T^2 + v_i^2\right)}, \qquad (8)$$

whereby the integration over velocities is reduced to summation of a few residues [17–19].

We assume that the energy difference $|1\rangle$ and $|2\rangle$ is much smaller than that between $|1\rangle$ and $|3\rangle$ (see parameters in Fig. 2). Thus, k_p can be regarded as the same as k_c (setting $k_p = k_c \equiv k$) and the integrations in $\langle \cdots \rangle_{xz}$ are reduced to

FIG. 3. Brightness $B(\delta_p, \theta, \infty)$ under different widths of the Doppler broadening (kv_T) plotted as a function of δ_p/γ_{31} and the angle θ. Data in panel (a) are obtained under $kv_T = 10\gamma_{31}$, (b) $kv_T = 5\gamma_{31}$, and (c) $kv_T = \gamma_{31}$. The other parameters are the same as in Fig. 2.
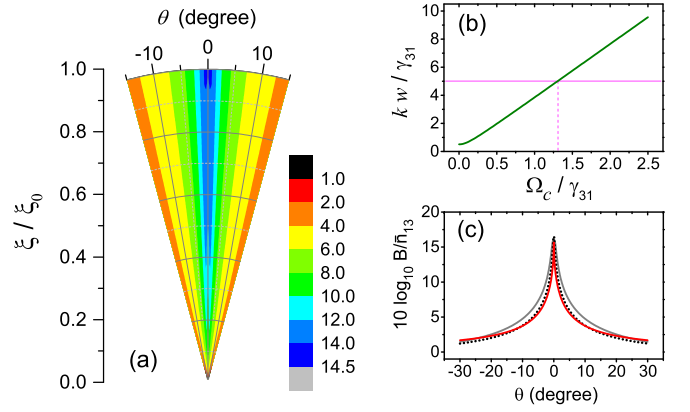
the contribution of four poles in the lower complex plane: $v_x = -iv_T$, $v_z = -iv_T$, $v_z = -i\frac{\gamma_{32}}{2k}$, and $v_z = -iw$. The last pole comes from the population distribution determined by the strong-coupling field, and it takes the form

$$w = \frac{1}{k}\sqrt{\frac{\gamma_{32}^2}{4} + \frac{\mathscr{B}}{\mathscr{A}}\Omega_c^2}, \qquad (9)$$

with $\mathscr{A} = 4[\Gamma_{32}R_{13} + (\Gamma_{31} + 3R_{13})R_{23}]$, and $\mathscr{B} = \gamma_{32}(\Gamma_{31} + 3R_{13})$. Under the condition $\Omega_c \gg \frac{\gamma_{32}}{2}\sqrt{\mathscr{A}/\mathscr{B}}$, we have $kw = \Omega_c\sqrt{\mathscr{B}/\mathscr{A}}$ [$kw = \Omega_c\sqrt{\gamma_{32}/4(R_{13} + R_{23})}$, if $\Gamma_{31} = \Gamma_{32}$ and $R_{ij} \ll \Gamma_{ij}$], with w measuring how large Ω_c is. The above linear relation is shown in Fig. 4(b), with $kw = 5\gamma_{31}$ marked by the pink horizontal line. For our system, this corresponds to approximately $\Omega_c = 1.3\,\gamma_{31}$. Roughly speaking, the pole of $-iv_T$ corresponds to the detrimental effect of the thermal motion on opening the EIT window, while the pole of $-iw$ represents the effort of the coupling field to overcome it. When $w \gtrsim v_T$ an adequate EIT window opens up [17]. We notice, however, that for $w \gtrsim 10\,v_T$, the Lorentzian lineshape no longer provides a reasonable approximation to the Gaussian lineshape.

Now, let us focus on the steady-state resonant brightness $B_0(\theta) = B(0, \theta, \infty)$. While the full expression for the brightness obtained using the Lorentzian lineshape is too bulky to be shown here, if we only focus on a small range of θ where a significant amount of output radiation falls ($\sin\theta \approx \theta$ and $\cos\theta \approx 1$), assuming that $kv_T > \gamma_{ij} \gg \gamma_0$ and $\frac{\gamma_{ij}}{2} < kw < 2kv_T$, the dominant terms in the expression reduce to

$$B_0 = \bar{n}_{13}\frac{\Gamma_{31}\bar{n}_{13} + \Gamma_{32}(\bar{n}_{23} + 1) + \mathscr{R}|\theta|(\bar{n}_{23} + 1 + \mathscr{N})}{\Gamma_{31}\bar{n}_{13} + \Gamma_{32}(\bar{n}_{23} - \bar{n}_{13}) + \mathscr{R}|\theta|(\bar{n}_{23} - \bar{n}_{13} + \mathscr{N})}, \qquad (10)$$

where

$$\mathscr{R} = \frac{8\Gamma_{32}kw(kv_T)^2}{\gamma_{32}\Omega_c^2}, \qquad (11)$$

and

$$\mathscr{N} = \frac{\gamma_{32}}{\Gamma_{32}}\left(\frac{\Omega_c^2}{4\,kv_T\,kw} + \frac{w + v_T}{w}|\theta|\right). \qquad (12)$$

Figure 4(c) shows the relative brightness $B_0/\bar{n}_{13}$ obtained from Eq. (10) with the red solid line. The *numerical* results from Eq. (7) with f_G (gray solid line) and f_L (black dotted line) are presented as well for comparison. In this regime of parameters, the brightness expressed by Eq. (10) is an excellent approximation of the full results obtained with a Lorentzian lineshape, while in turn the latter results compare quite well with the one corresponding to the Gaussian lineshape.

The analytical form of Eq. (10), with the introduction of the $\mathscr{R}$ and $\mathscr{N}$ quantities, allows us to easily consider the two cases of negligible and important Doppler effects. In the limit $|\theta| \to 0$, i.e., for the output along the same direction as the coupling laser which corresponds to a Doppler-free EIT Λ configuration, the brightness given by Eq. (10) reduces to Eq. (8) in Harris's paper [8]. When the Doppler broadening is important, instead, the terms proportional to $\mathscr{R}|\theta|$ become dominant ($\mathscr{R}|\theta| \gg \Gamma_{32}, \Gamma_{31}$, corresponding to $|\theta| \gtrsim 1°$ for

the parameters given in Fig. 2), then we have

$$B_0 \approx \bar{n}_{13}\frac{\bar{n}_{23} + 1 + \mathscr{N}}{\bar{n}_{23} - \bar{n}_{13} + \mathscr{N}}. \qquad (13)$$

It is noticeable that, defining a new parameter $\bar{n}'_{23} = \bar{n}_{23} + \mathscr{N}$, one can write B_0 as

$$B_0 \approx \bar{n}_{13}\frac{\bar{n}'_{23} + 1}{\bar{n}'_{23} - \bar{n}_{13}}, \qquad (14)$$

which is the same form as Eq. (10) in Ref. [8]. In other words, the Doppler effect acts as if the thermal occupation number of the reservoir that plays the role of the entropy sink is increased, or equivalently that the parameter $\bar{n}'_{23} > \bar{n}_{23}$ translates into a higher effective temperature $T'_{23} > T_{23}$ for this reservoir. While B_0 can indeed be much larger than the thermal occupation number $\bar{n}_{13}$ of the reservoir that plays the role of the energy source, it is always smaller than the maximum value allowed by the second law of thermodynamics owing to the presence of $\mathscr{N}$. This is shown in Fig. 5(a), where the brightness from Eq. (10) is compared with that obtained from Eq. (13) (for this choice of emission angle, $\mathscr{R}|\theta| \gtrsim \Gamma_{32}, \Gamma_{31}$) and with the ideal quantum heat engine limit as given by Eq. (19) below.

IV. THE ENTROPY BALANCE, POWER, AND EFFICIENCY

To assess how close to an ideal engine the Doppler-broadened engine can be, we proceed by examining its behavior in terms of the entropy balance. We adopt the asymptotic brightness $B(\delta_p, \theta, \infty)$ as the thermal occupation number to obtain the entropy flow rate per unit power; this is, the reciprocal of the radiation's flux temperature T_B [9,20,21]:

$$T_B^{-1} = \frac{K_b}{\hbar\omega_{31}}\frac{\int d\theta \int d\delta_p\,[(B+1)\ln(B+1) - B\ln B]}{\int d\theta \int d\delta_p\,B}, \qquad (15)$$

where K_b is the Boltzmann constant. The radiation flux temperature accounts for both emission energy and emission angle (see Fig. 3) in the count of the (averaged) entropy flow rate. Here the integration over δ_p and over θ are carried out numerically, spanning a range several FWHMs of the emission peak and adopting a Gaussian-broadening profile $f_G(v_i)$. Then, the entropy of the emitted radiation can be written as

$$S = \frac{\hbar\omega_{31}}{T_B}. \qquad (16)$$

Under the influence of the two thermal reservoirs at T_{13} (energy source), T_{23} (entropy sink) and the coupling laser (Ω_c), our system undergoes *both* processes

$$|1\rangle \xrightarrow{T_{13}} |3\rangle \xrightarrow{B} |1\rangle, \qquad (a)$$

$$|1\rangle \xrightarrow{T_{13}} |3\rangle \xrightarrow{T_{23}} |2\rangle \xrightarrow{\Omega_c} |3\rangle \xrightarrow{B} |1\rangle, \qquad (b)$$

the latter representing a quantum heat engine cycle. Without the coupling, the output only comes from process (a) so that, for a thermal (detailed) balance $B = n_{13}$, as determined by the
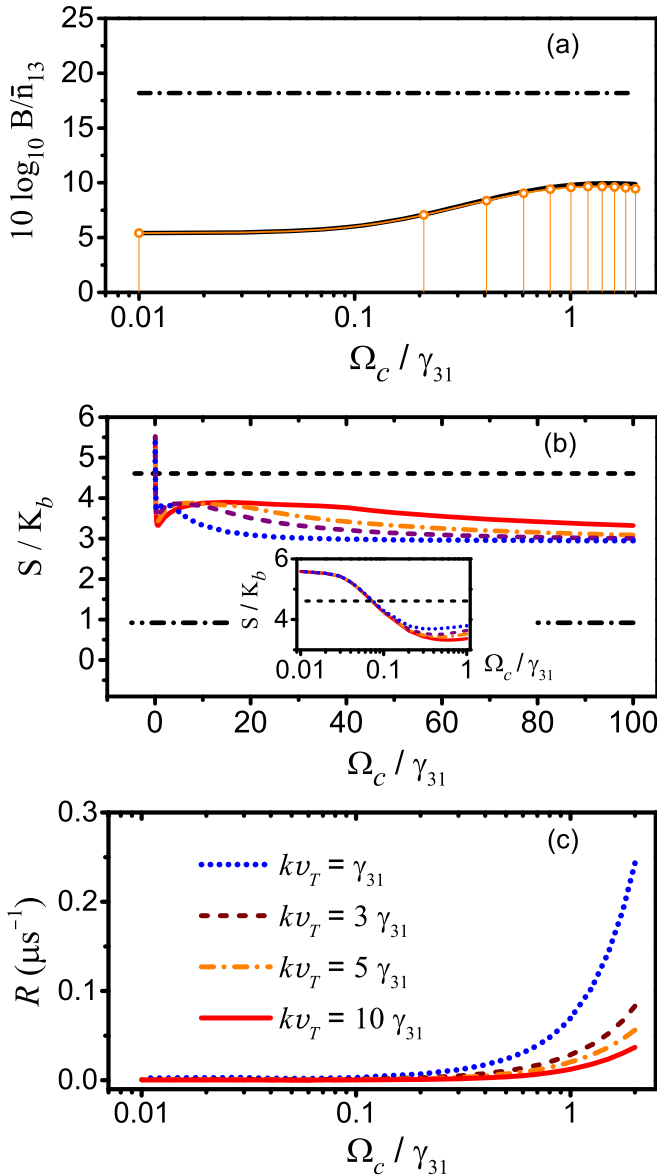
FIG. 5. (a) $B_0(\theta = 1°)$ from Eq. (10) (black solid line) and from Eq. (13) (orange circle marked line), the horizontal dash-dotted line corresponds to the ideal quantum heat engine. Here $kv_T = 5\,\gamma_{31}$. (b) Entropy of the output radiation under different Doppler broadenings $kv_T = \gamma_{31}$ (blue dotted line), $3\,\gamma_{31}$ (purple dashed line), $5\,\gamma_{31}$ (orange dash-dotted line), and $10\,\gamma_{31}$ (red solid line). The horizontal dashed line and the horizontal dash-dotted line indicate, respectively, the limits due to the thermodynamics inequalities of Eq. (18) (blackbody reservoir only) and Eq. (19) (ideal quantum heat engine). (c) Emission rates of the output plotted for $kv_T = \gamma_{31}$, $3\gamma_{31}$, $5\gamma_{31}$, and $10\,\gamma_{31}$ are plotted with respect to Ω_c. The same correspondence between line style and value of kv_T as in panel (b) is used here, and other parameters are identical to those in Fig. 2.

blackbody reservoir at T_{13}, the entropy balance of (a) is

$$S - \frac{\hbar\omega_{31}}{T_{13}} \geqslant 0. \qquad (18)$$

In process (b), i.e., the quantum heat engine process, the ideal laser does not contribute to the entropy balance, and the

entropy balance for (b) is instead

$$S - \frac{\hbar\omega_{31}}{T_{13}} + \frac{\hbar\omega_{32}}{T_{23}} \geqslant 0, \qquad (19)$$

where the equality corresponds to an ideal engine; the grade of the work provided by the output photons is in this case the highest possible [8].

Figure 5(b) shows the numerical results for the entropy S of the output field from Eqs. (15) and (16) under different widths of Doppler broadening. For weak-coupling fields, as shown in the inset, the entropy lies above the horizontal dashed line which is $\hbar\omega_{31}/K_B T_{13}$, process (a) being the dominant one. Increasing the value of Ω_c, the line of S crosses the horizontal dashed line indicating that process (b) becomes indeed effective and the system behaves like a quantum heat engine. The nonmonotonic behavior of S is found to depend on the integration range of Eq. (15), as determined by the shape of the brightness peak. For even-larger values of Ω_c, the output becomes brighter and process (b) starts to dominate: The entropy of the output decreases below the blackbody limit of process (a) (horizontal dashed), yet remaining above the minimal value (horizontal dash-dotted) allowed by the thermodynamics of an ideal heat engine process. For larger widths of Doppler broadening, the engine entropy balance moves away from the ideal limit (horizontal dash-dotted) and towards the no-coupling process (a) (horizontal dashed), suggesting that the engine is increasingly hampered for increasingly large linewidths.

The engine's total emission rate R, namely, the number of output photons generated per second [8,23], obtained by integrating the asymptotic brightness over frequency and emission angle, is

$$R = \frac{1}{2\pi} \iint B(\delta_p, \theta, \infty) d\delta_p d\theta, \qquad (20)$$

with $B(\delta_p, \theta, \infty)$ given in Fig. 3. We plot R in Fig. 5(c) as a function of the coupling's Rabi frequency for four different broadenings. For a fixed value of Ω_c, the asymptotic brightness $B(\delta_p, \theta, \infty)$ at larger angles drops down quickly for increasing values of Doppler broadening since the engine is more sensitive to θ at larger kv_T (see Fig. 3) and the engine is now hampered with a corresponding increase of n'_{23}. This behavior of the angular distribution of the output manifests itself in the emission rate in Fig. 5(c): The total power gets smaller under large broadenings for a given coupling intensity. On the other hand, for a fixed value of the Doppler broadening, the total emission rate R increases with Ω_c since the width of the brightness peak gets wider, while the peak height $[B(0, 0, \infty)]$ remains constant and equal to the Doppler-free case.

We finally turn to the engine efficiency, noting that the engine's total output energy per second is

$$P_{\text{out}} = \frac{\hbar}{2\pi} \iint (\omega_{31} + \delta_p) B(\delta_p, \theta, \infty) d\delta_p d\theta. \qquad (21)$$

Considering the symmetry of $B(\delta_p, \theta, \infty)$ over δ_p and θ, the double integral yields $P_{\text{out}} = \hbar\omega_{31} R$, as for the Doppler-free case. Confining ourselves to the quantum heat engine cycle [process (b)], it is clear that generating an output photon means absorbing one photon from reservoir T_{13} and one

photon from the coupling field. Then, the engine's efficiency η is taken here as the ratio [8] of the overall output energy $\hbar\omega_{31} R \Delta t$ to the total input energy $(\hbar\omega_{31} + \hbar\omega_{32})R \Delta t$ during the interval Δt, i.e.,

$$\eta = \frac{\omega_{31}}{\omega_{31} + \omega_{32}}, \tag{22}$$

suggesting the same efficiency for both Doppler-broadened and Doppler-free heat engines.

V. CONCLUSIONS

Quantum heat engines may also work with coherently driven Doppler-broadened atomic samples, albeit with a reduced brightness when compared with Doppler-free samples [8]. Their behavior has been characterized in terms of entropy balance, efficiency, and power, providing detailed quantitative results through numerical and analytical treatments showing anisotropy in the brightness of the generated radiation with a sharp decrease as we misalign from the coupling beam. The effect of broadening may be foreseen as an increment of the thermal occupation number of the reservoir acting as entropy sink [Eqs. (13) and (14)]. Our findings suggest that it is feasible to make quantum heat engines work with routine warm atoms platforms, which are simpler and more convenient to manipulate than those so far realized with ultracold atomic samples [10].

[1] J. G. Bohnet, Z. Chen, J. M. Weiner, K. C. Cox, and J. K. Thompson, Linear-response theory for superradiant lasers, Phys. Rev. A **89**, 013806 (2014).

[2] J. J. Longdell, E. Fraval, M. J. Sellars, and N. B. Manson, Stopped Light with Storage Times Greater Than One Second Using Electromagnetically Induced Transparency in a Solid, Phys. Rev. Lett. **95**, 063601 (2005).

[3] Y.-F. Hsiao, P.-J. Tsai, H.-S. Chen, S.-X. Lin, C.-C. Hung, C.-H. Lee, Y.-H. Chen, Y.-F. Chen, I. A. Yu, and Y.-C. Chen, Highly Efficient Coherent Optical Memory Based on Electromagnetically Induced Transparency, Phys. Rev. Lett. **120**, 183602 (2018).

[4] I. Iakoupov, J. Borregaard, and A. S. Sørensen, Controlled-Phase Gate for Photons Based on Stationary Light, Phys. Rev. Lett. **120**, 010502 (2018).

[5] K. Liao, H. Yan, J. He, S. Du, Z.-M. Zhang, and S.-L. Zhu, Subnatural-Linewidth Polarization-Entangled Photon Pairs with Controllable Temporal Length, Phys. Rev. Lett. **112**, 243602 (2014).

[6] C. R. Murray and T. Pohl, Coherent Photon Manipulation in Interacting Atomic Ensembles, Phys. Rev. X **7**, 031007 (2017).

[7] O. Lahad and O. Firstenberg, Induced Cavities for Photonic Quantum Gates, Phys. Rev. Lett. **119**, 113601 (2017).

[8] S. E. Harris, Electromagnetically induced transparency and quantum heat engines, Phys. Rev. A **94**, 053859 (2016).

[9] X. L. Ruan, S. C. Rand, and M. Kaviany, Entropy and efficiency in laser cooling of solids, Phys. Rev. B **75**, 214304 (2007).

[10] Y. Zou, Y. Jiang, Y. Mei, X. Guo, and S. Du, Quantum Heat Engine using Electromagnetically Induced Transparency, Phys. Rev. Lett. **119**, 050602 (2017).

[11] A. Safari, I. De Leon, M. Mirhosseini, O. S. Magaña Loaiza, and R. W. Boyd, Light-Drag Enhancement by a Highly Dispersive Rubidium Vapor, Phys. Rev. Lett. **116**, 013601 (2016).

[12] S. Zhang, Y. Hu, G. Lin, Y. Niu, K. Xia, J. Gong, and S. Gong, Thermal-motion-induced non-reciprocal quantum optical system, Nat. Photonics **12**, 744 (2018).

[13] G. Lin, S. Mang, Y. Hu, Y. Niu, J. Gong, and S. Gong, Nonreciprocal Amplification with Four-Level Hot Atoms, Phys. Rev. Lett. **123**, 033902 (2019).

[14] D.-W. Wang, H.-T. Zhou, M.-J. Guo, J.-X. Zhang, J. Evers, and S.-Y. Zhu, Optical Diode Made from a Moving Photonic Crystal, Phys. Rev. Lett. **110**, 093901 (2013).

[15] M.-X. Dong, K.-Y. Xia, W.-H. Zhang, Y.-C. Yu, Y.-H. Ye, E.-Z. Li, L. Zeng, D.-S. Ding, B.-S. Shi, G.-C. Guo, and F. Nori, All-optical reversible single-photon isolation at room temperature, Sci. Adv. **7**, eabe8924 (2021).

[16] L. Zhu, X. Guo, C. Shu, H. Jeong, and S. Du, Bright narrowband biphoton generation from a hot rubidium atomic vapor cell, Appl. Phys. Lett. **110**, 161101 (2017).

[17] A. Javan, O. Kocharovskaya, H. Lee, and M. O. Scully, Narrowing of electromagnetically induced transparency resonance in a Doppler-broadened medium, Phys. Rev. A **66**, 013805 (2002).

[18] O. Kocharovskaya, Y. Rostovtsev, and M. O. Scully, Stopping Light Via Hot Atoms, Phys. Rev. Lett. **86**, 628 (2001).

[19] E. Kuznetsova, O. Kocharovskaya, P. Hemmer, and M. O. Scully, Atomic interference phenomena in solids with a long-lived spin coherence, Phys. Rev. A **66**, 063802 (2002).

[20] L. Landau, On the thermodynamics of photoluminescence, J. Phys. USSR **10**, 503 (1946).

[21] C. E. Mungan, Radiation thermodynamics with applications to lasing and fluorescent cooling, Am. J. Phys. **73**, 315 (2005).

[22] D. Mihalas and B. W. Mihalas, *Foundations of Radiation Hydrodynamics* (Oxford University Press, New York, 1984).

[23] A. Imamoglu, J. E. Field, and S. E. Harris, Lasers without Inversion: A Closed Lifetime Broadened System, Phys. Rev. Lett. **66**, 1154 (1991).